Fast calculation of a family of elliptical mass gravitational lens models

Rennan Barkana[1]
Institute for Advanced Study, School of Natural Sciences, Princeton, NJ 08540

ABSTRACT

Because of their simplicity, axisymmetric mass distributions are often used to model gravitational lenses. Since galaxies are usually observed to have elliptical light distributions, mass distributions with elliptical density contours offer more general and realistic lens models. They are difficult to use, however, since previous studies have shown that the deflection angle (and magnification) in this case can only be obtained by rather expensive numerical integrations. We present a family of lens models for which the deflection can be calculated to high relative accuracy (10^{-5}) with a greatly reduced numerical effort, for small and large ellipticity alike. This makes it easier to use these distributions for modelling individual lenses as well as for applications requiring larger computing times, such as statistical lensing studies. A program implementing this method can be obtained from the author[2].

Subject headings: gravitational lensing — cosmology — galaxies: structure

1. Introduction

The types of density profiles used to model gravitational lenses have been motivated by observations of lenses in addition to practical considerations. Observed features of galaxies and clusters that can be incorporated into lens models include ellipticity and radially decreasing mass density profiles. But it is essential to be able numerically to calculate quickly the deflection angle and magnification of a light ray due to a lens model, in order to probe the entire range of parameter space when searching for a best fit to an observed lens. Numerical efficiency is even more important in cases with multiple sources such as radio lenses observed at high resolution. Strongly lensed arcs in clusters sometimes lie near cluster galaxies and thus modelling all the lensed features in a cluster may require a combination of many individual lenses. Another application which depends on numerical speed is the statistical study of properties of the images of a lens model for comparison with lens surveys.

---

[1]email: barkana@ias.edu

[2]or at http://www.sns.ias.edu/~barkana/ellip.html

In attempting to construct models that are as realistic as possible, new features must be introduced carefully, since in a single case of multiple lensing there are a small number of constraints requiring a small number of model parameters. Ellipticity adds just two parameters (magnitude and orientation), and it appears to be essential. Galaxies and clusters often appear elliptical, with significant numbers having axis ratios b/a smaller than 0.5. Axisymmetric lens models are also excluded by many observed lens systems, in which the images are not colinear with the lens position on the sky. Of course, the asymmetry in each case may also be due in part to external shear from other nearby galaxies or from large-scale structure along the line of sight (Bar-Kana 1996, Keeton et al. 1997).

However, the use of elliptical mass distributions has not become common practice because the evaluation of the deflection angle and magnification matrix requires some effort. Bourassa et al. (1973) and Bourassa and Kantowski (1975) (with minor corrections by Bray (1984)) introduced a complex formulation of lensing which allows for an elegant expression of the deflection angle due to a homoeoidal elliptical mass distribution. I.e., this is a projected, two dimensional mass distribution whose isodensity contours are concentric ellipses of constant ellipticity and orientation. It can be obtained, e.g., by projecting a three-dimensional homoeoidal mass distribution. The complex integral which gives the deflection angle is in practice difficult to separate into real and imaginary parts. Schramm (1990) used an alternative derivation to obtain the deflection without the use of complex numbers, but still requiring a numerical integral for each component of the deflection angle. Elliptical densities have been used for numerical lens modelling, with the ellipticity allowed to vary in order to fit the data, by Keeton & Kochanek (1997).

In order to avoid numerical integration, several alternatives have been suggested to exact elliptical mass distributions. Models where the potential is chosen to have elliptical contours rather than the density are easy to use, since the deflection can be obtained immediately as the gradient of the potential. The imaging properties of elliptical potentials have been investigated extensively (Kovner 1987, Blandford & Kochanek 1987 and Kochanek & Blandford 1987). They become identical to elliptical densities for very small ellpticities and produce similar image configurations even for moderate ellipticty (Kassiola & Kovner 1993, hereafter KK93). However, elliptical potentials cannot represent mass distributions with axis ratios b/a smaller than about 0.5 because the corresponding density contours acquire the artifical feature of a dumbbell shape, and the density can also become negative in some cases (Kochanek & Blandford 1987, KK93). To avoid this problem, Schneider & Weiss (1991) proposed a numerical method based on a multipole expansion of the mass distribution, but this expansion converges slowly when used with large ellipticity.

In this paper we consider a family of projected density profiles that has been used with the approximate approaches to ellipticity discussed above. This is the family of softened power-law profiles, which have a constant density within a core radius and approach a power-law fall-off at large radii. In §2 we introduce our notation for softened power-law elliptical mass distributions (SPEMDs) and for softened power-law elliptical potentials (SPEPs), and illustrate further the limitations of SPEPs. In §3 we present and simplify the quadrature solution of Schramm (1990) for the deflection angle. We show that for the SPEMDs it is possible to approximate the integrand so that the integral can be done analytically. Although the result is a sum of series expansions, each series converges rapidly to high accuracy, even for mass densities with arbitrarily high ellipticity. We show how to similarly evaluate the magnification matrix. We also derive an expression for the gravitational potential, but it cannot be evaluated without a numerical integration. Finally, in §4 we summarize our results.

2. SPEMDs and SPEPs

Consider a projected mass density Σ at an angular diameter distance D_d and a source at D_s, with a distance of D_{ds} from the lens to the source. Then the lens equation can be written as

$$\mathbf{y} = \mathbf{x} - \alpha(\mathbf{x}) \tag{1}$$

where $\mathbf{y}$ is the source angle, $\mathbf{x} = (x_1, x_2)$ is the observed image angle, and $\alpha = (\alpha_1, \alpha_2)$ is the deflection angle scaled by a factor of D_{ds}/D_s (see e.g. Schneider et al. 1992 for an introduction to gravitational lensing). The deflection is

$$\alpha(\mathbf{x}) = \nabla\psi(\mathbf{x}), \tag{2}$$

in terms of the potential

$$\psi(\mathbf{x}) = \frac{1}{\pi}\int d^2x'\kappa(\mathbf{x}')\ln|\mathbf{x}-\mathbf{x}'| \ . \tag{3}$$

Equation 3 is the solution to the Poisson equation

$$\nabla^2\psi(\mathbf{x}) = 2\kappa(\mathbf{x}) \ , \tag{4}$$

where $\kappa = \Sigma/\Sigma_{cr}$ in terms of the critical density

$$\Sigma_{cr} = \frac{c^2}{4\pi G}\frac{D_s}{D_d D_{ds}} \ . \tag{5}$$

The SPEMD is given by

$$\kappa(\rho) = \left[\frac{\rho^2 + s^2}{E^2}\right]^{\frac{\eta}{2}-1} \ , \tag{6}$$

where s is the core radius, η is the power-law index, and E fixes the overall normalization. The dependence on position is through

$$\rho^2 = x_1^2 + x_2^2/\cos^2\beta \ , \tag{7}$$

where $\cos\beta$ is the axis ratio b/a and the ellipticity is $e = 1 - \cos\beta$. The parameter η can vary from a modified Hubble profile ($\eta = 0$) through isothermal ($\eta = 1$) to a constant surface density sheet ($\eta = 2$).

The SPEP is specified by a potential

$$\psi(\rho_p) = \frac{2E_p^2}{\eta^2}\left[\frac{\rho_p^2+s_p^2}{E_p^2}\right]^{\frac{\eta}{2}} \quad , \tag{8}$$

where

$$\rho_p^2 = x_1^2 + x_2^2/\cos^2\beta_p \ . \tag{9}$$

The corresponding density as specified by the Poisson equation (4) is

$$\kappa_p = \frac{1}{\eta}\left[\frac{\rho_p^2+s_p^2}{E_p^2}\right]^{\frac{\eta}{2}-1}\left\{(\eta-2)\frac{x_1^2+x_2^2/\cos^4\beta_p}{\rho_p^2+s_p^2} + \left(1+\frac{1}{\cos^2\beta_p}\right)\right\} \ . \tag{10}$$

For $\rho_p \gg s_p$, the axis ratio of this density distribution is

$$A_p = \cos\beta_p\left[\frac{1+(\eta-1)\cos^2\beta_p}{\eta-\sin^2\beta_p}\right]^{\frac{1}{\eta-2}} \tag{11}$$

(Equivalent forms for κ_p and A_p have been derived by KK93 and Grogin and Narayan (1996), respectively). KK93 have shown that the isodensity contours acquire a concave part and become dumbbell shaped when $\cos^2\beta_p < 1 - \eta/3$. Thus for a given η the requirement of convex density contours implies a smallest axis ratio A_p that can be represented, or equivalently a maximum ellipticity of

$$e_{\max}(\eta) = 1 - \sqrt{1-\frac{\eta}{3}}\left(2-\frac{\eta}{2}\right)^{\frac{1}{\eta-2}} \quad . \tag{12}$$

Figure 1 plots this maximum ellipticity as a function of η, and shows that $e_{\max}$ is typically around 0.5. An ellipticity greater than 0.65 cannot be modelled for any $\eta < 2$.

Assigning corresponding parameters between the SPEP and the SPEMD is somewhat arbitrary, but we follow KK93 and use the following conventions. For zero core radius and zero ellipticity, we require the SPEP and SPEMD to match, which yields the condition $E = E_p$. We require the density axis ratios b/a far from the core to be equal, i.e. $\cos\beta = A_p$. Finally, we also require the central densities to match (if the core radii are nonzero), which yields

$$s = s_p\left[\frac{1+\cos^2\beta_p}{\eta\cos^2\beta_p}\right]^{\frac{1}{\eta-2}} \quad .$$

Figure 1 shows that at a fixed η, as the ellipticity is increased the contours of the SPEP become dumbbell shaped at the critical value $e_{\max}(\eta)$. This is illustrated in Figure 4 of KK93, which shows the density contours of several pairs of corresponding SPEMDs and SPEPs, for several values of b/a and with η fixed at 1. Figure 2 illustrates the complementary case, where if we decrease η at a fixed ellipticity the contours switch over from being convex to having the dumbbell shape. Figure 2a shows the isodensity contours of an SPEMD with axis ratio $b/a = 0.5$. For simplicity, we set the core radius equal to zero. For the SPEMD, the contour shape depends only on the axis ratio

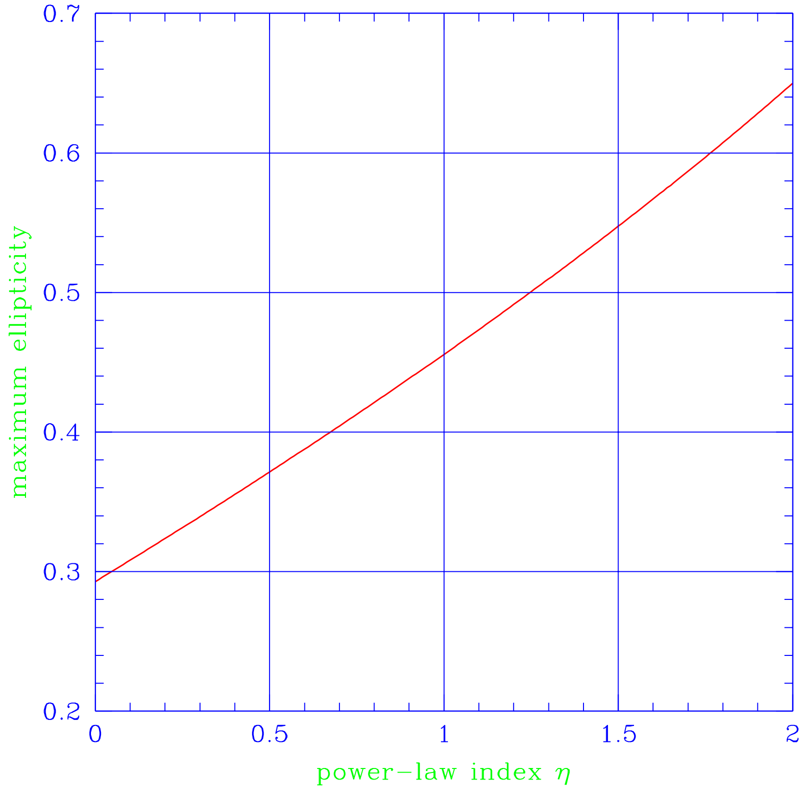

Fig. 1.— Maximum ellipticity representable by an SPEP model shown as a function of the power-law index η.

and is independent of η. Figure 2b shows the isodensity contours of the corresponding SPEP with $\eta = 1.6$ and the same axis ratio of 0.5 for the density contours. As we decrease η keeping the axis ratio fixed, the SPEP contours remain convex until the value of $\eta = 1.25$ shown in Figure 2c, but they become dumbbell shaped below this as illustrated in Figure 2d for $\eta = 0.4$.

Even with the problem of the SPEP regarding isodensity contour shape, it is of interest to directly compare the lensing behaviour of the two models, the SPEP and SPEMD. We compare them in the same configuration as KK93, i.e. for a source placed directly behind the center of the lens. In this case there are four images, with two images on the y-axis at $(0, \pm y)$ with magnification A_y and two on the x-axis at $(\pm x, 0)$ with magnification A_x. Figure 7 of KK93 shows the distance ratio x/y and the magnifications A_x and A_y for the SPEMD and corresponding SPEP, as a function of ellipticity for the singular (i.e. zero core) isothermal profile. In figure 3 we plot the distance ratio y/x and the magnification ratio A_y/A_x for singular profiles with $\eta = 0.5$, $\eta = 1$, and $\eta = 1.5$. The

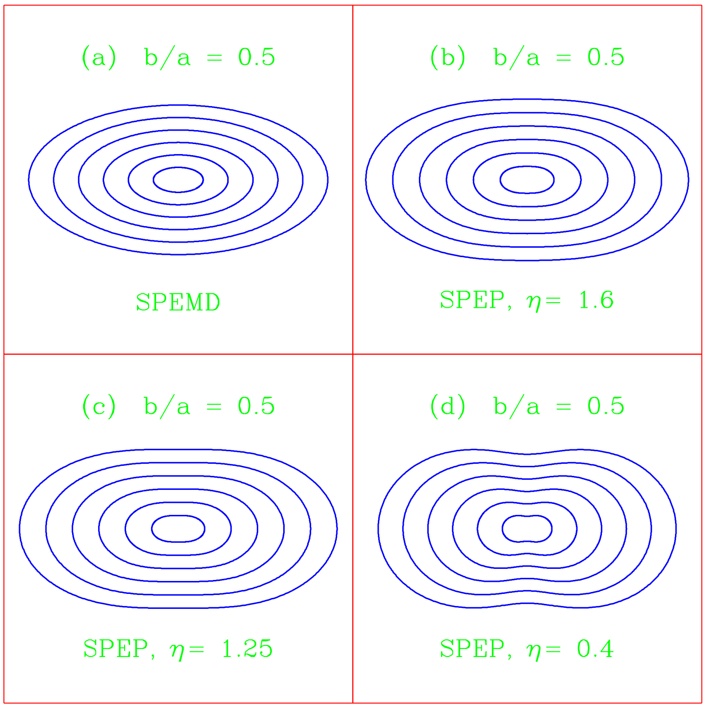

Fig. 2.— Isodensity contours of SPEMDs and corresponding SPEPs. Panel (a) shows the SPEMD contours with axis ratio 0.5. For a fixed axis ratio, as we decrease η the SPEP contours switch from convex to dumbbell shaped, as shown in panels (b), (c), and (d).

distance ratios behave similarly for the SPEMD (solid curves) and SPEP (dashed curves), though there are small differences at high ellipticity. The magnification ratio is an observable, not the individual image magnifications, and we find that the behavior of the magnification ratio at high ellipticity differs significantly between the SPEMD and SPEP even at $\eta = 1$, but more so at smaller η. Thus while the SPEP produces some image configurations qualitatively similar to those of the SPEMD, quantitatively it is not an accurate substitute unless the ellipticity is small.

3. The deflection angle, magnification matrix, and potential of the SPEMD

We begin with the solution of Schramm (1990) for any elliptical density of the form $\kappa(\rho)$, which we write concisely as

$$\begin{aligned}
\alpha_1(x_1,x_2) &= 2x_1 \cos\beta \int_0^{\rho(x_1,x_2)} \frac{\rho'\kappa(\rho')\,\omega}{x_1^2+\omega^4\,x_2^2} d\rho' \ , \\
\alpha_2(x_1,x_2) &= 2x_2 \cos\beta \int_0^{\rho(x_1,x_2)} \frac{\rho'\kappa(\rho')\,\omega^3}{x_1^2+\omega^4\,x_2^2} d\rho' \ , \\
\omega^2 &\equiv \frac{\Delta + r^2 + \rho'^2 \sin^2\beta}{\Delta + r^2 - \rho'^2 \sin^2\beta} \ , \\
\Delta^2 &\equiv \left[\rho'^2 \sin^2\beta + x_2^2 - x_1^2\right]^2 + 4x_1^2x_2^2 \ ,
\end{aligned} \tag{13}$$

where $r^2 = x_1^2 + x_2^2$. The upper limit of integration $\rho(x_1, x_2)$ is given by equation (7). In what follows we can restrict x_1 and x_2 to be nonnegative without loss of generality, noting from equations (13) that $\alpha_1(x_1,x_2) = \alpha_1(|x_1|,|x_2|)\,\mathrm{sign(x_1)}$ and $\alpha_2(x_1,x_2) = \alpha_2(|x_1|,|x_2|)\,\mathrm{sign(x_2)}$.

To simplify Δ, we switch variables to

$$\mu = \frac{\rho'^2 \sin^2\beta + x_2^2 - x_1^2}{2x_1x_2} \ . \tag{14}$$

We find that ω^2 factorizes as $\omega^2 = (\mu + \sqrt{\mu^2+1})\,x1/x2$, which is a key point for our method below to work. If we write κ as a function of μ, i.e. $\bar\kappa(\mu) \equiv \kappa(\rho)$, we obtain

$$\begin{aligned}
\alpha_1(x_1,x_2) &= \frac{\cos\beta\sqrt{x_1x_2}}{\sin^2\beta} \int_{\mu_1}^{\mu_2} \bar\kappa(\mu) f(\mu) d\mu \ , \\
\alpha_2(x_1,x_2) &= \frac{\cos\beta\sqrt{x_1x_2}}{\sin^2\beta} \int_{\mu_1}^{\mu_2} \bar\kappa(\mu) f(-\mu) d\mu \ , \\
f(\mu) &\equiv \sqrt{\frac{1}{\sqrt{1+\mu^2}} - \frac{\mu}{\mu^2+1}} \ , \\
\mu_1 &\equiv \frac{1}{2}\left(\frac{x_2}{x_1} - \frac{x_1}{x_2}\right) \ , \\
\mu_2 &\equiv \frac{1}{2}\left(\frac{x_2}{x_1\cos^2\beta} - \frac{x_1\cos^2\beta}{x_2}\right) \ .
\end{aligned} \tag{15}$$

This analysis so far is correct for any density of the form $\kappa(\rho)$. We now specialize to the SPEMD, which we can write as $\bar\kappa(\mu) = \bar q(\mu + \bar s)^{-\gamma}$. In terms of our variables from §2, we have $\gamma = 1 - \eta/2$, $\bar q = [2x_1x_2/(E^2 \sin^2\beta)]^{-\gamma}$, and $\bar s = -\mu_1 + s^2\sin^2\beta/(2x_1x_2)$. Defining $\nu \equiv \mu + \bar s$, we finally obtain

$$\begin{aligned}
\alpha_1(x_1,x_2) &= \tilde q I_1 \ , \\
\alpha_2(x_1,x_2) &= \tilde q I_2 \ ,
\end{aligned} \tag{16}$$

in terms of a common factor

$$\widetilde{q} = \frac{\cos\beta\sqrt{x_1 x_2}}{\sin^2\beta}\bar{q} \tag{17}$$

and the integrals

$$\begin{aligned} I_1 &= \int_{\nu_1}^{\nu_2} \nu^{-\gamma} f(\nu - \bar{s}) d\nu \ , \\ I_2 &= \int_{\nu_1}^{\nu_2} \nu^{-\gamma} f(\bar{s} - \nu) d\nu \ , \end{aligned} \tag{18}$$

evaluated between the limits

$$\nu_1 = \frac{s^2\sin^2\beta}{2x_1x_2} \ ; \qquad \nu_2 = \nu_1 + \frac{\sin^2\beta}{2}\left(\frac{x_1}{x_2} + \frac{x_2}{x_1\cos^2\beta}\right) \ . \tag{19}$$

To evaluate the integral I_1 we make use of the fact that $f(\mu)$ depends only on the variable μ and we know its functional form, so we can approximate $f(\nu - \bar{s})$ as a polynomial in either ν or $1/\nu$ for various ranges of ν from 0 to ∞ (the lower limit ν_1 in I_1 is always nonnegative). After some experimentation, we settle on a number of strategies for these polynomial expansions.

For a small range of μ values around 0, e.g. μ_a to μ_b, we use Chebyshev polynomials (see e.g. Press et al. 1992) to construct a polynomial approximation for $f(\mu)$ of the form $\sum_{n=0}^{n=N} c_n\mu^n$. Then we can evaluate the portion of I_1 between $\nu_a = \mu_a + \bar{s}$ and $\nu_b = \mu_b + \bar{s}$ to be (e.g. if γ is not an integer)

$$\int_{\nu_a}^{\nu_b} \nu^{-\gamma}\sum_{n=0}^{n=N} c_n(\nu - \bar{s})^n d\nu = \sum_{n=0}^{n=N}\sum_{m=0}^{m=n} \frac{c_n n!}{m!(n-m)!}\frac{(-\bar{s})^{n-m}}{m+1-\gamma}\left(\nu_b^{m+1-\gamma} - \nu_a^{m+1-\gamma}\right) \ .$$

We can reduce the number of computations if $\bar{s} \gg |\mu_b - \mu_a|$, because we can then write $\nu^{-\gamma} = \bar{s}^{-\gamma}[1 + (\nu - \bar{s})/\bar{s}]^{-\gamma}$, expand this in powers of $(\nu - \bar{s})/\bar{s}$, and use $\nu - \bar{s}$ as the variable of integration. The advantage of using Chebyshev polynomials is that the expansion converges rapidly if the range of μ values is not too large.

For $\mu \gg 1$, we expand $f(\mu)$ in inverse powers of μ,

$$f(\mu) \approx \frac{1}{\sqrt{2}\mu^{3/2}} - \frac{5}{8\sqrt{2}\mu^{7/2}} \ . \tag{20}$$

Consider just the first term (we deal similarly with the second term). We can write a contribution to I_1 in this regime as

$$\int_{\nu_a}^{\nu_b} \nu^{-\gamma}\frac{d\nu}{\sqrt{2}(\nu - \bar{s})^{3/2}} = \frac{1}{\sqrt{2}}|\bar{s}|^{-\gamma-1/2}\int_{\nu_a/|\bar{s}|}^{\nu_b/|\bar{s}|} \bar{\nu}^{-\gamma}\frac{d\bar{\nu}}{(\bar{\nu} - \bar{u})^{3/2}} \ ,$$

where we have set $\bar{\nu} \equiv \nu/|\bar{s}|$ and $\bar{u} \equiv \mathrm{sign}(\bar{s})$ is ± 1. Then if $\bar{\nu} \gg 1$, we expand

$$(\bar{\nu} - \bar{u})^{-3/2} = \bar{\nu}^{-3/2}\left(1 + \frac{3\bar{u}}{2\bar{\nu}} + \frac{15}{8\bar{\nu}^2} + \dots\right)$$

and then integrate. On the other hand, for small values of $\bar{\nu}$ up to a few we can again use Chebyshev polynomial approximation, this time for the function $(\bar{\nu}-\bar{u})^{-3/2}$, and then integrate (we do this separately for the two signs of $\bar{u}$). In practice we find that it is better to perform an integration by parts and then use a polynomial approximation for the function $(\bar{\nu}-\bar{u})^{-1/2}$ instead. When $\bar{u}=+1$ we cannot extend this down to $\bar{\nu}=1$, so for a range of $\bar{\nu}$ near 1 we leave $(\bar{\nu}-1)^{-3/2}$ unchanged but Taylor expand the $\bar{\nu}^{-\gamma}$ term about $\bar{\nu}=1$. The result is an integrand which is a sum of powers of $\bar{\nu}-1$ and is easily integrated. When $\bar{u}=-1$, we find that we sometimes need high accuracy near $\bar{\nu}=0$, so for a small range of $\bar{\nu}\ll 1$ we Taylor expand $(\bar{\nu}+1)^{-3/2}$ about the midpoint of this narrow range, and then integrate.

We use the same set of methods when $(-\mu)\gg 1$, but here the expansion is

$$f(\mu)\approx\frac{\sqrt{2}}{\sqrt{-\mu}}-\frac{3}{4\sqrt{2}(-\mu)^{5/2}}\ . \tag{21}$$

In some cases we can use other methods to increase the speed. If the entire integration range of I_1 is narrow, i.e. $(\nu_2-\nu_1)\ll 1$, then we Taylor expand $f(\nu-\bar{s})$ about the midpoint of the range and then integrate, without breaking up this range into the various regimes described above.

The required accuracy determines how we specify the various regimes. We were motivated by the lens 0957+561 (e.g. Walsh et al. 1979, Young et al. 1981, Falco et al. 1991, Grogin & Narayan 1996), where VLBI observations (Porcas et al. 1981, Gorenstein et al. 1988, Garret et al. 1994) require a relative accuracy in the deflection angle of one part in 10^5. For algorithmic simplicity we prefer to use only two terms in the expansions (20) and (21), so this high accuracy forces us to use them only for $|\mu|>15.7$. For $-15.7<\mu<15.7$ we use the direct Chebyshev expansion of $f(\mu)$. We find it best to break up this range into 7 intervals and construct a Chebyshev expansion in each, with the number of terms in the expansions ranging from 6 to 9, keeping the relative accuracy roughly constant.

The integral I_2 is evaluated using exactly the same expansions as I_1 but with $f(-\mu)$ substituted for $f(\mu)$. The components of the 2×2 inverse magnification matrix $\delta_{ij}-\partial\alpha_i/\partial x_j$ also yield similar integrals. Using equations (16) through (19) we derive

$$\begin{aligned}
\frac{\partial\alpha_1}{\partial x_1} &= \left(\frac{1}{2}-\gamma\right)\frac{\alpha_1}{x_1}+\tilde{q}\left[\nu_2^{-\gamma}f(\nu_2-\bar{s})\frac{\partial\nu_2}{\partial x_1}-\nu_1^{-\gamma}f(\nu_1-\bar{s})\frac{\partial\nu_1}{\partial x_1}-I_3\frac{\partial\bar{s}}{\partial x_1}\right]\ ,\\
\frac{\partial\alpha_2}{\partial x_2} &= \left(\frac{1}{2}-\gamma\right)\frac{\alpha_2}{x_2}+\tilde{q}\left[\nu_2^{-\gamma}f(\bar{s}-\nu_2)\frac{\partial\nu_2}{\partial x_2}-\nu_1^{-\gamma}f(\bar{s}-\nu_1)\frac{\partial\nu_1}{\partial x_2}+I_4\frac{\partial\bar{s}}{\partial x_2}\right]\ ,\\
\frac{\partial\alpha_2}{\partial x_1} &= \frac{\partial\alpha_1}{\partial x_2}=\left(\frac{1}{2}-\gamma\right)\frac{\alpha_1}{x_2}+\tilde{q}\left[\nu_2^{-\gamma}f(\nu_2-\bar{s})\frac{\partial\nu_2}{\partial x_2}-\nu_1^{-\gamma}f(\nu_1-\bar{s})\frac{\partial\nu_1}{\partial x_2}-I_3\frac{\partial\bar{s}}{\partial x_2}\right]\ .
\end{aligned} \tag{22}$$

Just as with I_1 and I_2, we evaluate the integrals

$$\begin{aligned}
I_3 &= \int_{\nu_1}^{\nu_2}\nu^{-\gamma}f'(\nu-\bar{s})d\nu\ ,\\
I_4 &= \int_{\nu_1}^{\nu_2}\nu^{-\gamma}f'(\bar{s}-\nu)d\nu\ ,
\end{aligned} \tag{23}$$

where we approximate $f'(\mu) \equiv df(\mu)/d\mu$ in the same ways as we created polynomial approximations for $f(\mu)$ above. The other quantities appearing in equations (22) can be evaluated (for $i = 1$ and 2) as

$$\begin{aligned} \frac{\partial \nu_1}{\partial x_i} &= -\frac{\nu_1}{x_i} \; ; \qquad \frac{\partial \bar{s}}{\partial x_i} = \frac{\partial \nu_1}{\partial x_i} - \frac{1}{2x_i}\left[\frac{x_1}{x_2} + \frac{x_2}{x_1}\right](-1)^i \\ \frac{\partial \nu_2}{\partial x_i} &= \frac{\partial \nu_1}{\partial x_i} - \frac{\sin^2\beta}{2x_i}\left[\frac{x_1}{x_2} - \frac{x_2}{x_1\cos^2\beta}\right](-1)^i \; . \end{aligned} \tag{24}$$

If we apply the same amount of computational effort to I_3 and I_4 as for I_1 and I_2, we nevertheless find that the relative accuracy is lower for the magnification $\det^{-1}|\delta_{ij} - \partial\alpha_i/\partial x_j|$ than it is for the components of α, for a couple reasons. First, the various polynomial expansions tend to converge more slowly for $f'(\mu)$ than for $f(\mu)$; and second, the components of α are directly proportional to I_1 and I_2, but in equations (22) we sometimes have to subtract nearly equal terms and get a low accuracy for $\partial\alpha_i/\partial x_j$ even if I_3 and I_4 are evaluated accurately. In practice we achieve a maximum relative error of 5×10^{-6} for α and 6×10^{-4} for the magnification, and a typical relative error of 1×10^{-6} for α and 5×10^{-5} for the magnification. A higher accuracy is not needed for the magnification, given typical measurement errors on fluxes.

In terms of running time, with the above accuracy we can evaluate the deflection angle and magnification matrix of the SPEMD roughly 20 times faster than the brute force method (which requires 5 integrals), although this is still about 15 times slower than the SPEP, or any other model with the deflection given by a simple formula. This speedup should make the SPEMD model useful for applications in which repeated numerical integrations made it previously unusable.

To evaluate the gravitational part of the time delay, we also need to evaluate the potential $\psi(\mathbf{x})$. Schramm (1990) gives a quadrature expression for the potential of a single elliptical shell. We obtain the potential of any elliptical density $\kappa(\rho)$ by integrating over shells,

$$\psi(x_1, x_2) = \cos\beta \int_{\rho'=0}^{\rho(x_1,x_2)} \int_{u=0}^{\gamma(\rho')} \frac{du}{\sqrt{(\rho'^2 + u)(\rho'^2\cos^2\beta + u)}} \rho'\kappa(\rho')d\rho' \; , \tag{25}$$

where

$$\gamma(\rho') = \frac{1}{2}\left\{r^2 - \rho'^2(1 + \cos^2\beta) + \Delta\right\} \tag{26}$$

in terms of the last equation of (13). Performing the inner integral, we derive

$$\psi(x_1, x_2) = 2\cos\beta \int_{\rho'=0}^{\rho(x_1,x_2)} \ln\left[\frac{\sqrt{\Delta + r^2 - \rho'^2\sin^2\beta} + \sqrt{\Delta + r^2 + \rho'^2\sin^2\beta}}{\sqrt{2}\rho'(1 + \cos\beta)}\right] \rho'\kappa(\rho')d\rho' \; . \tag{27}$$

In this case the integrand does not factorize when we substitute equation (14), so the potential must be numerically integrated and cannot be speeded up. In most applications, though, it is not necessary to evaluate the potential a large number of times.

4. Conclusions

A mass density profile with elliptical isodensity contours is a natural lens model to try when axisymmetric models fail. Previously, however, the easiest way of evaluating the deflection has been to numerically integrate the solutions of Schramm (1990). After simplifying these solutions we have shown that for the family of SPEMD mass distributions, the deflection angle and magnification matrix can be evaluated very fast and with high accuracy. Our implementation achieves a relative accuracy of 5×10^{-6} in the deflection and 6×10^{-4} in the magnification while running 20 times faster than a procedure based on the numerical integrations. We have also derived an expression for the potential, although this quantity must be numerically integrated.

As noted by Schneider & Weiss (1991), combinations of two or more SPEMDs with different parameters can be used to construct more general density profiles with several scales. We thus expect SPEMDs to be more widely used, particularly for cases of high ellipticity in which the alternative SPEPs develop the artificial feature of dumbbell-shaped contours.

I thank Ed Turner for valuable discussions. This work was supported by Institute Funds.

REFERENCES

Bar-Kana, R. 1997, ApJ, 468, 17

Blandford , R. D., & Kochanek, C. S. 1987, ApJ, 321, 658

Bourassa, R. R., & Kantowski, R. 1975, ApJ, 195, 13

Bourassa, R. R., Kantowski, R., & Norton, T. D. 1973, ApJ, 185, 747

Bray, I. 1984, MNRAS, 208, 511

Falco, E. E., Gorenstein, M. V., & Shapiro, I. I. 1991, ApJ, 372, 364

Gorenstein, M. V., Cohen, N. L., Shapiro, I. I. Rogers, A. E. E., Bonometti, R. J., Falco, E. E., Bartel, N, & Marcaide, J. M. 1988, ApJ, 334, 42

Grogin, N. A., & Narayan, R. 1996a, ApJ, 464, 92; erratum, ApJ, 473, 570

Kassiola, A., & Kovner, I. 1993, ApJ, 417, 450 (KK93)

Keeton, C. R., & Kochanek, C. S. 1997, ApJ, 487, 42

Keeton, C. R., Kochanek, C. S., & Seljak, U. 1997, ApJ, 482, 604

Kochanek, C. S., & Blandford, R. D. 1987, ApJ, 321, 676

Kovner, I. 1987, Nature, 325, 507

Porcas, R. W., Booth, R. S., Browne, I. W. A., Walsh, D., & Wilkinson, P. N. 1981, Nature, 289, 758

Press, W. H., Teukolsky, S. A., Vetterling, W. T., & Flannery, B. P. 1992, Numerical Recipes in Fortran: The Art of Scientific Computing, Sec. Edition (New York: Cambridge Univ. Press)

Schneider, P., Ehlers, J., & Falco, E.E. 1992, Gravitational Lenses (New York: Springer)

Schneider, P., & Weiss, A. 1991, A&A, 247, 269

Schramm, T. 1990, A&A, 231, 19

Walsh, D., Carswell, R. F., & Weymann, R. J. 1979, Nature, 279, 381

Young, P., Gunn, J. E., Kristian, J., Oke, J. B., & Westphal, J. A. 1981, ApJ, 244, 736

This preprint was prepared with the AAS LaTeX macros v4.0.

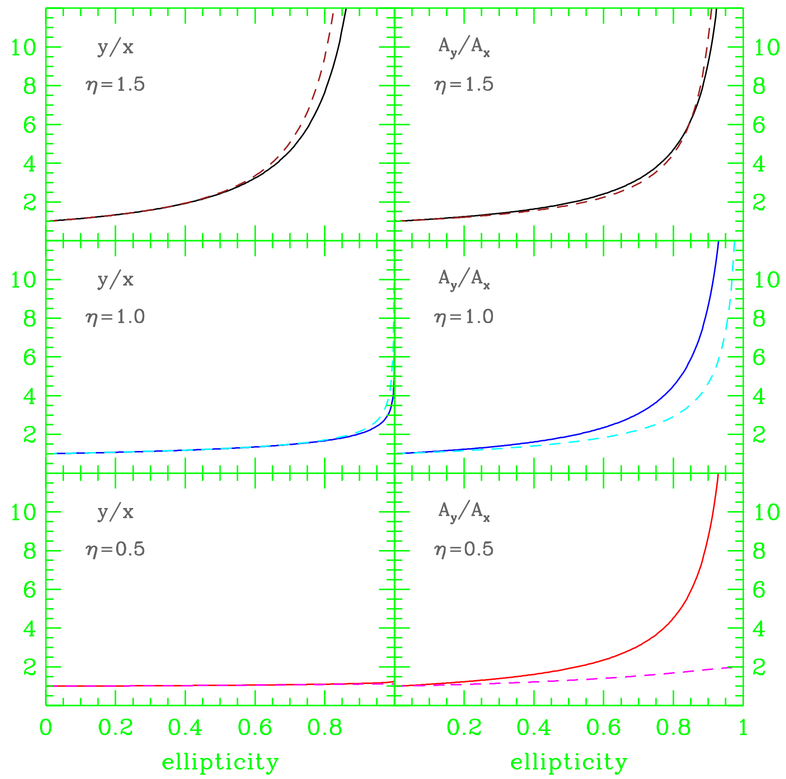

Fig. 3.— Properties of the four images of a source placed directly behind the lens center, for SPEMDs and corresponding SPEPs. Several different power-law indices η are considered. The panels on the left show the distance y of the images on the y-axis over the distance x of the images on the x-axis, and the panels on the right show the magnification ratio A_y/A_x of the two types of images. In each case the appropriate quantity is plotted as a function of ellipticity, with the SPEMD as the solid curve and the SPEP as the dashed curve.